

Forcing function control of Faraday wave instabilities in viscous shallow fluids

Cristián Huepe (1), Yu Ding (2), Paul Umbanhowar (2) and Mary Silber (1)

(1) *Department of Engineering Sciences and Applied Mathematics.*

(2) *Department of Physics and Astronomy. Northwestern University,
2145 Sheridan Road, Evanston, IL 60208-3112, USA*

(Dated: August 31, 2018)

We investigate the relationship between the linear surface wave instabilities of a shallow viscous fluid layer and the shape of the periodic, parametric-forcing function (describing the vertical acceleration of the fluid container) that excites them. We find numerically that the envelope of the resonance tongues can only develop multiple minima when the forcing function has more than two local extrema per cycle. With this insight, we construct a multi-frequency forcing function that generates at onset a non-trivial harmonic instability which is distinct from a subharmonic response to any of its frequency components. We measure the corresponding surface patterns experimentally and verify that small changes in the forcing waveform cause a transition, through a bicritical point, from the predicted harmonic short-wavelength pattern to a much larger standard subharmonic pattern. Using a formulation valid in the lubrication regime (thin viscous fluid layer) and a WKB method to find its analytic solutions, we explore the origin of the observed relation between the forcing function shape and the resonance tongue structure. In particular, we show that for square and triangular forcing functions the envelope of these tongues has only one minimum, as in the usual sinusoidal case.

PACS numbers: 47.35.+i, 47.20.-k, 47.54.+r

I. INTRODUCTION

In the Faraday system, an incompressible fluid is oscillated vertically in a container with a free upper surface, generating standing surface waves which provide an excellent system for the study of pattern formation [1, 2]. Through an appropriate choice of experimental parameters, many of the regular patterns that are possible in two dimensions, such as stripes, squares and hexagons, can be obtained. In addition, targets, spirals, superlattices and quasipatterns lacking strict translational periodicity have also been observed [3, 4, 5, 6, 7].

One of the advantages of the Faraday experiment, when compared to other pattern-forming systems such as convection or chemical reactions, is the great amount of control over the energy feeding mechanism that can be achieved by changing the periodic vertical acceleration of the fluid container. Even by forcing the system with different combinations of only two frequencies, several distinct patterns can be achieved. Hexagonal and rhomboid patterns, together with various quasipatterns have been obtained experimentally in [8, 9, 10] by varying the amplitudes and the phase difference between both components. Superlattice patterns [11, 12], triangular patterns [13] and localized structures [14] have also been observed using two-frequency forcings [15].

From a theoretical perspective, a combination of tools must be used to understand and predict the pattern selection. While its characteristic wavelength can be obtained through a linear instability calculation, the two-dimensional structure is determined by the nonlinear interaction between modes [16, 17, 18, 19, 20, 21, 22, 23, 24]. At the linear level, the simplest cases occur when a deep fluid layer of low viscosity is oscillated with a sinusoidal forcing, i.e. proportional to $\sin(\omega t)$. In these situ-

ations, the frequency of the main (largest in amplitude) component of the resulting surface wave oscillations will be $\omega/2$ (referred to hereafter as the first -or fundamental-subharmonic response). In other cases, two mechanisms for selecting the main frequency responses that are different from the first subharmonic one have been identified.

The first mechanism occurs when two or more frequency components are introduced in the forcing. In these cases, each component will tend to excite its own corresponding first subharmonic mode. Their relative amplitudes will determine which of these responses has the lowest global forcing strength threshold, thus becoming the instability that is observed at onset. The second mechanism can only arise in the high viscosity regime. If the fluid layer is shallow enough, even a single component forcing with low enough frequency can excite an instability different from the first subharmonic one. As the viscous boundary layer reaches the bottom of the fluid container, the threshold of the lowest unstable modes rises, allowing others with higher main frequency components (and, therefore, shorter surface wavelengths) to become unstable at onset [25, 26].

In a numerical and experimental study, it was shown in [27] that a transition between two patterns with different linearly unstable wavelengths can be obtained in various fluid regimes by changing the relative amplitudes of a two-frequency forcing function. This transition occurs through a bicritical point, where both modes are simultaneously neutrally stable. In spite of these results, only a limited understanding of the effects of both a multi-frequency forcing and a high viscosity regime has been achieved. Furthermore, little is known about the patterns expected for more complicated forcing functions not described by a few frequency components. This can be attributed to the essentially infinite number of degrees

of freedom that are needed to parametrize an arbitrary forcing function, which renders a systematic exploration of the parameter space impossible.

In this paper, we consider a different and novel approach. Instead of exploring a large parameter space with various forcing frequency components, we seek to identify which characteristics of the periodic forcing function affect the surface patterns and how. By performing a numerical linear stability calculation in various test systems of shallow viscous fluid layers, we will first identify a simple qualitative relation between the shape of the forcing function and the resonance tongue structure (that describes the stability thresholds). Using this relation, we will construct a forcing function with a non-trivial critical instability at onset, having a main frequency component which does not correspond to the fundamental subharmonic (or even the fundamental harmonic) response to any of its forcing frequencies. We will then present experimental results showing the surface pattern generated by this instability. Finally, in the lubrication limit of a thin viscous fluid layer, we will illustrate analytically the origin of the observed relation between the forcing function and the stability thresholds. We will follow the method introduced by Cerda and Tirapegui [28, 29] that derives a Mathieu equation to describe this regime and uses a WKB approximation [30, 31] to solve it for single frequency forcing. By extending these calculations to arbitrary forcing functions we will develop an intuitive understanding of the relation between the shape of the forcing function and the structure of the resonance tongues. In particular, we will show that only forcing functions with more than two local extrema per cycle are expected to allow bicritical points involving non-contiguous tongues.

The paper is organized as follows. In Section II we review the standard formulation of the Faraday wave linear stability analysis. We introduce in Section III a one-parameter family of forcing functions to illustrate numerically the relation between the shape of each member of the family and the structure of its corresponding neutral stability diagram. Section IV presents an experimental study that uses these forcing functions, displaying a previously unobserved transition between two surface patterns with very different characteristic wavelengths. In Section V we show an approximate analytical relation between the forcing and the instability response that illuminates our approach. Finally, Section VI briefly discusses our results and presents our conclusions.

II. BACKGROUND

We study the linear stability of the free surface of an incompressible Newtonian fluid layer of depth h , density ρ , kinematic viscosity ν and surface tension σ . The fluid is oscillated vertically with acceleration $f(\omega t)$, where ω is the fundamental frequency of oscillation and t is the time. We will summarize here the derivation of the equations describing this system by following the presentation in

[32].

Using the incompressibility condition to eliminate the pressure in the linearized Navier-Stokes equation we obtain

$$(\partial_t - \nu \nabla^2) \nabla^2 u_z = 0, \quad (1)$$

where $u_z(x, y, z, t)$ is the vertical component of the fluid velocity. In an idealized laterally infinite container, the horizontal eigenfunctions are given by $e^{\pm i\vec{k}\cdot\vec{r}}$, with $\vec{r} = (x, y)$ and $\vec{k} = (k_x, k_y)$. For each surface wavenumber $k = |\vec{k}|$, equation (1) thus becomes

$$[\partial_t - \nu(\partial_{zz} - k^2)] (\partial_{zz} - k^2) v_k = 0, \quad (2)$$

where $v_k(z, t)$ describes the z -dependence of u_z associated with the mode k . In the oscillating reference frame with $z = 0$ at the flat fluid surface, the boundary conditions on the bottom of the container are given by

$$v_k = 0 \quad \text{and} \quad \partial_z v_k = 0, \quad \text{at} \quad z = -h. \quad (3)$$

At the fluid surface, the vertical position of the free boundary $z = \xi_k(t)e^{i\vec{k}\cdot\vec{r}}$ associated to every mode k is advected by the fluid motion. To linear order in the surface deformation this kinematic boundary condition is

$$\frac{d\xi_k}{dt} = v_k \quad \text{at} \quad z = 0. \quad (4)$$

Additional boundary conditions are imposed at the surface by finding the total balance of forces tangential and normal to the interface. From this we obtain

$$(\partial_{zz} + k^2) v_k = 0, \quad (5)$$

$$[\partial_t - \nu(\partial_{zz} - k^2) + 2\nu k^2] \partial_z v_k = [g(1 + \Gamma f(\omega t)) + \frac{\rho}{\sigma} k^2] k^2 \xi_k, \quad (6)$$

at $z = 0$,

where g is the gravitational acceleration and f is a non-dimensional function defined to have $\max(|f(\omega t)|) = 1$. Therefore, Γ corresponds to the maximum acceleration of the forcing function, expressed in units of g .

Equation (2) and boundary conditions (3) through (6) fully describe the dynamics of the system. Instead of integrating them directly, our numerical analysis will focus on finding the stability threshold $\Gamma_c(k)$ given by the critical value of Γ at which the wavenumber k becomes unstable.

III. NUMERICAL STUDY

A. Method

We are interested in finding numerically the neutral stability curve $\Gamma_c(k)$ for various forcing functions. With this objective, we have extended the stability analysis

method of Kumar and Tuckerman [27, 32] to forcing functions with an arbitrary number of frequency components. In broad terms, this method consists first in expanding v_k and ξ_k in a Floquet form

$$v_k = e^{(\mu+i\phi)t} \sum_j w_j(z) e^{ij\omega t} + c.c. \quad (7)$$

$$\xi_k = e^{(\mu+i\phi)t} \sum_j \zeta_j e^{ij\omega t} + c.c.. \quad (8)$$

Here, $\mu + i\phi$ is the Floquet exponent, where we can set the growth rate μ to 0 to obtain marginal stability curves with harmonic ($\phi = 0$) and subharmonic ($\phi = \omega/2$) temporal responses. Equations (2)-(5) are then used to rewrite (6) in the form

$$A_n \zeta_n = \Gamma [f\zeta]_n, \quad (9)$$

where A_n is an algebraic function of the system parameters, which does not depend on $f(\omega t)$, and $[f\zeta]_n$ is the n -th Fourier component of

$$f(\omega t) \sum_j \zeta_j e^{ij\omega t}. \quad (10)$$

By introducing the explicit form of $f(\omega t)$, equation (9) can be expressed as an eigenvalue problem for the forcing amplitude Γ which can then be solved through standard numerical techniques. In order to extend the method to cases beyond the two-frequency forcing computed in [27, 32], we implemented this algorithm in *Mathematica* [33] and used the program's symbolic algebra capabilities to automatically compute $[f\zeta]_n$ for any given $f(\omega t)$. With this implementation, which is analogous to that presented in [34], we are able to obtain efficiently the neutral stability curves for any desired forcing function, regardless of its frequency content.

B. Results

We restrict our study to shallow viscous fluid layers. Since the specific value of the fluid constants within this regime does not change our qualitative results or analysis, we will further reduce the size of the parameter space by considering throughout the paper only one set of fluid constants. These are given by a density $\rho = 0.95 \text{ g/cm}^3$, a surface tension $\sigma = 20 \text{ dyn/cm}$ and a viscosity $\nu = 46 \text{ cS}$. Additionally, we will use in this section and in Section IV a fluid depth $h = 0.3 \text{ cm}$ and an oscillation frequency $\omega = 2\pi (10 \text{ Hz})$.

By using the numerical techniques described above, we explored the structure of the marginal stability curves $\Gamma_c(k)$ for many different $f(\omega t)$ including various piecewise constant, piecewise linear, delta-like and multi-frequency functions. While a precise characterization of how the features of $f(\omega t)$ correlate to those of $\Gamma_c(k)$ remains to be achieved, one of the salient qualitative relations that we observed for all tested functions is a connection between the extrema of $f(\omega t)$ and the envelope

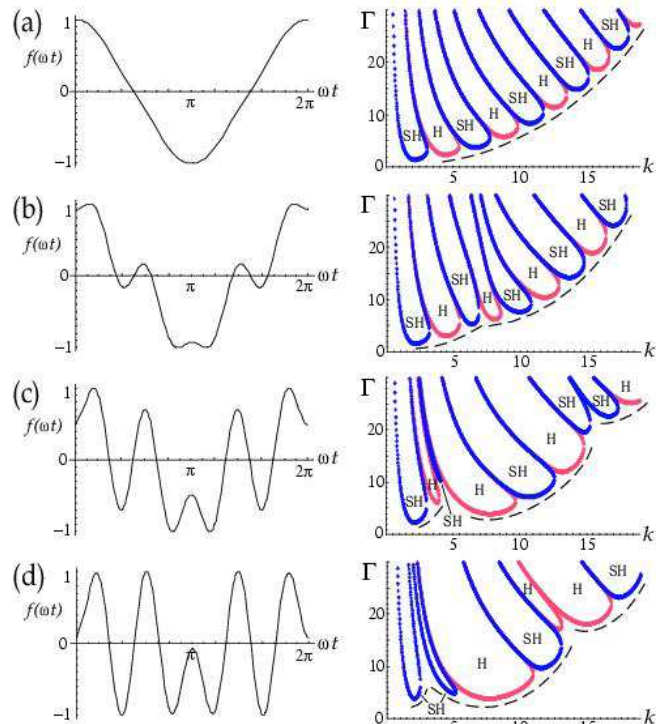


FIG. 1: (Color online) Shape of the forcing functions (left) defined in (11) and their corresponding neutral stability curves (right) for (a) $p = -2$, (b) $p = -0.3$, (c) $p = 0.5$, (d) $p = 1$, and parameters $\rho = 0.95 \text{ g/cm}^3$, $\sigma = 20 \text{ dyn/cm}$, $\nu = 46 \text{ cS}$, $\omega = 2\pi (10 \text{ Hz})$ and $h = 0.3 \text{ cm}$. Γ is in units of g and k in cm^{-1} . The resonance tongues labeled H and SH show regions with harmonic or subharmonic linear instabilities, respectively. Note how their envelopes (dashed lines) change with p .

of $\Gamma_c(k)$ that will be described below. We will illustrate it here for a specific family of forcing functions, which is the same as that in the experiments of Section IV.

Consider the following set of forcing functions parametrized by p

$$f_p(\omega t) = \mathcal{N} [2.5 \cos(\omega t) + 3^p \cos(3\omega t) - 5^p \cos(5\omega t)], \quad (11)$$

where ω is the fundamental frequency of oscillation and \mathcal{N} is a normalization constant which is defined so that $\max(|f_p(\omega t)|) = 1$. The specific form of (11) is an arbitrary choice which is not important for the qualitative behavior that we will focus on here. It was obtained by searching for a one-parameter family of forcing functions that simultaneously includes members with a simple triangular-like form ($p \approx -2$) and others that can produce non-trivial surface-wave instabilities in an experimentally accessible regime ($p \approx 1$).

Figure 1 displays in the left column $f_p(\omega t)$ for $p = -2$, $p = -0.3$, $p = 0.5$ and $p = 1$. The right column shows the corresponding neutral stability curves $\Gamma_c(k)$ which present the usual resonance tongue structure. The harmonic and subharmonic tongues indicate

regions where surface waves become unstable, oscillating with a main frequency component that is an integral multiple ($\omega, 2\omega, 3\omega, \dots$) or an odd half-multiple ($\omega/2, 3\omega/2, 5\omega/2, \dots$) of the fundamental forcing frequency, respectively. The tongues at higher k -values correspond to instabilities with shorter surface wavelengths and higher oscillation frequencies. As p is increased, the forcing function changes from a simple rounded triangular shape with only two extrema per cycle to shapes with richer structure. Correspondingly, the envelope defined by the tongue minima (sketched as a dashed line on the figure) changes from a simple convex function with a single minimum to a set of convex segments, each with its own minimum.

We have observed a similar relation between the structure of the extrema of $f(\omega t)$ and the concavity of the resonance tongue's envelope for all forcing functions tested (triangular, square, multi-frequency, etc.) In particular, every $f(\omega t)$ with only two extrema per cycle resulted in an envelope with positive concavity for all k . This relation will be one of our main focuses in the remainder of this paper.

It is important to point out that the changes in the critical instabilities illustrated in Fig. 1 cannot be explained by a simple switch to a different dominant forcing frequency in $f_p(\omega t)$ combined with the first mechanism described in the Introduction. Indeed, as p is increased to 1 the lowest unstable region becomes the second harmonic tongue (with main frequency component equal to 2ω) which does not correspond to the fundamental harmonic or subharmonic responses (with equal or half the frequency, respectively) to any of the three frequency components of $f_p(\omega t)$: ω , 3ω and 5ω . Furthermore, it is apparent that the change in p cannot be characterized as mainly reducing the stability threshold of a specific tongue, but that it rather affects the aforementioned envelope over the entire range of k studied.

IV. EXPERIMENTAL RESULTS

In this section, we present experimental results showing that the appearance of multiple minima in the envelope of the resonance tongues can generate interesting measurable effects. By carefully choosing the form of the forcing function, we find a previously unobserved bicritical point between two surface patterns with very different characteristic wavelengths.

In our experiments, we use silicone oil with $\rho = 0.95 \text{ g/cm}^3$, $\sigma = 20 \text{ dyn/cm}$ and $\nu = 46 \text{ cS}$ (Fluka Silicone Oil AR 20), which are the same fluid parameters as in Section III. A 0.3 cm deep layer of this silicone oil is contained in a cylindrical cell with a radius of 7.0 cm and height of 4.0 cm. The cell has a PVC sidewall, a 0.8 cm thick glass bottom, and a 0.8 cm thick plexiglass top covered with a light diffuser. It is mounted on the ram of a $10 \times 10 \text{ cm}^2$ linear air bearing, which is attached to a 180 kg triangular granite slab that floats on an air

table to minimize horizontal oscillations. A shaker (VTS VG100) is suspended by springs from the air table supports. Two 50 cm long cylindrical aluminum tubes, each with an inner and outer diameter of 0.48 cm and 0.95 cm, respectively, connect the shaker to the ram. An amplifier (Crown CE2000) drives the shaker with a computer-generated forcing function. The amplitudes and phases of the desired Fourier components of the acceleration signal are measured by an accelerometer (PCB Model 353B68) and used as feedback to control the driving. The root-mean-square difference between the measured and target forcing functions is less than 1% while the variation in the amplitudes of the driven components is less than 0.01%. Since viscosity and surface tension are both sensitive to temperature changes, the experiments are conducted in a closed transparent box maintained at a constant temperature ($\pm 0.005^\circ\text{C}$). To visualize the waves, parallel light is projected through the cell bottom. The curved fluid surface refracts the light, which then falls on the diffuser producing a representation of the pattern. A CCD camera synchronized with the forcing function acquires the images.

Our specific choice of forcing function was determined by searching for an experimentally achievable set of parameters having a linear instability at onset with a response far from the usual subharmonic one. This objective is not easily achieved despite the fact that our numerical exploration established that many forcing functions generate resonance tongues with a multiple minima envelope. Indeed, for the fluid parameters used in our experiments, we found numerically that a tongue belonging to the second or higher (in order of increasing k) envelope minimum can be excited at onset only for very low values of h or ω . However, the range of these two quantities is limited by our experimental apparatus. For very shallow fluid layers ($h < 0.1 \text{ cm}$), spurious effects can affect the patterns: surface waves may contact the bottom of the container and a small tilt, variation in the bottom profile, or wetting at the wall can lead to large changes in the relative fluid depth $\Delta h/h$. Additionally, as h and ω are reduced, the critical acceleration Γ_c increases. Because the maximum acceleration and amplitude ($\propto \omega^{-2}$) of the apparatus are limited, much of this low ω /large Γ regime is inaccessible. By testing numerically various forcing functions, we were able to construct $f_p(\omega t)$ with $p \approx 1$, as defined in (11), which has a global minimum in the part of the envelope that does not contain the first subharmonic tongue (see Fig. 1d), and which is experimentally accessible.

Figure 2 displays the neutral stability curves computed numerically for the experimental parameters specified above, using $\omega = 2\pi$ (10 Hz) and a forcing $f_p(\omega t)$ with $p = 0.9$, $p = 1.0$ and $p = 1.1$. The figure shows a very small change in the forcing function (see left panels) producing a large jump in the critical wavenumber. For $p = 0.9$ (top), the first subharmonic tongue (with main frequency component at $\omega/2$) will be excited at onset. Numerically, we compute a critical forcing $\Gamma_c^{\text{SH}} = 3.35$

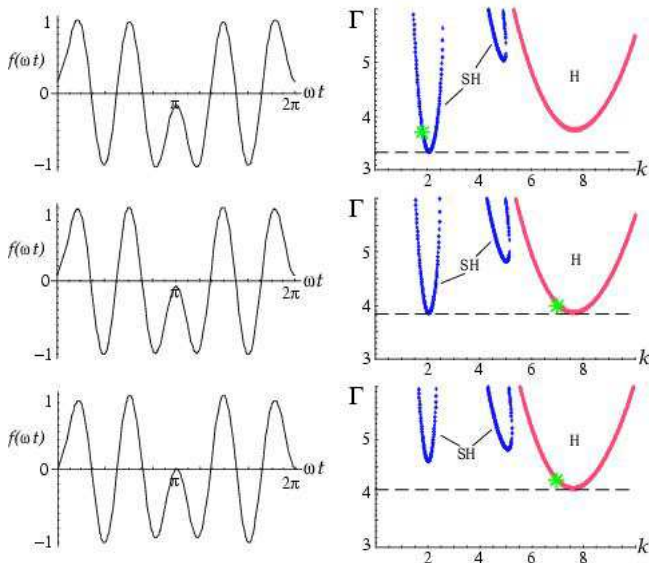


FIG. 2: (Color online) Shape of the forcing functions (left) and their corresponding neutral stability curves (right) for $p = 0.9$ (top), $p = 1.0$ (center), $p = 1.1$ (bottom), and the same parameters and units as in Fig. 1. For small changes in $f(\omega t)$, the instability at onset (occurring at critical forcings indicated by the dashed lines) switches from the first subharmonic (SH) resonance tongue to the second harmonic (H) one. Each asterisk indicates the critical forcing Γ_c and wavenumber k_c measured experimentally.

and a critical wavenumber $k_c^{\text{SH}} = 2.07$. At $p = 1.0$ (center), the system is close to a bicritical point, where the first subharmonic and second harmonic tongues become simultaneously unstable at onset. The corresponding critical values are $\Gamma_c^{\text{SH}} = 3.86$, $k_c^{\text{SH}} = 2.05$ and $\Gamma_c^{\text{H}} = 3.87$, $k_c^{\text{H}} = 7.64$, respectively. Finally, for $p = 1.1$ (bottom) the second harmonic tongue becomes the instability at onset, with $\Gamma_c^{\text{H}} = 4.10$ and $k_c^{\text{H}} = 7.59$. We refer to it as the second harmonic one since it oscillates with a main frequency component at 2ω , and is therefore the second harmonic tongue in order of growing k (the first being above the plotted Γ -range, between the two subharmonic tongues displayed). It is a non-trivial critical instability, which cannot be easily explained by the mechanisms described in the Introduction, because it does not correspond to the first harmonic or subharmonic responses to any of the forcing frequency components (ω , 3ω and 5ω). Instead, it is related to the second local minimum of the envelope of the resonance tongues (see Fig. 1d).

Experimentally, we observe the transition between these two linearly unstable regimes by using the same $f_p(\omega t)$ forcing function. Figure 3 shows images of the surface patterns for $p = 0.9$ (left) and $p = 1.1$ (right). As predicted by our numerical calculations, their characteristic length scale changes dramatically, in spite of the small variation in $f_p(\omega t)$. For $p = 0.9$, we obtain a pattern of large hexagons at a critical forcing $\Gamma_c = 3.72g$, with a characteristic size of 3.5 cm which corresponds to

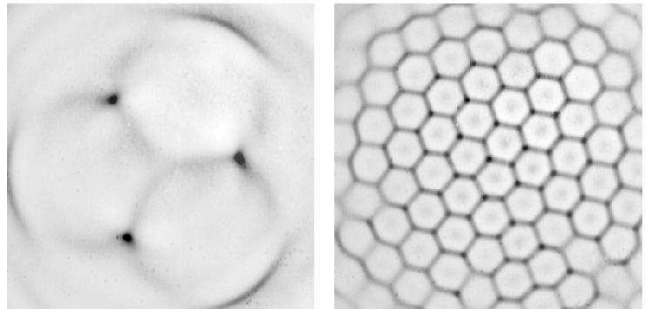


FIG. 3: Experimental pictures (negative-images) of the surface patterns appearing at onset for $p = 0.9$ (left) and $p = 1.1$ (right), corresponding to the top and bottom forcing functions in Fig. 2. Note that, for this small variation in the forcing, a dramatic change in the pattern is observed. The size of each image is 8.22 cm \times 8.22 cm, which captures the central region of the container.

the critical wavenumber $k_c = 1.77$. When compared to the numerical results, Γ_c is within 10% and k_c within 15% of the predicted values. Given the pattern deformation that is observed towards the image borders due to the small aspect ratio (the size of the container is only about twice the surface wavelength), these discrepancies are not significant. For $p = 1.1$, a pattern of small hexagons appears at $\Gamma_c = 4.27$, with a characteristic size of 0.9 cm, which implies $k_c = 6.96$. These measurements are within 4% (for Γ_c) and 9% (for k_c) of the numerical predictions. We have also verified in our experiments that, with respect to the fundamental forcing frequency, the oscillations of the large pattern are subharmonic and those of the small one are harmonic. Finally, at $p = 1.0$ (image not shown), we observe that the system generates small hexagons which are practically indistinguishable from those at $p = 1.1$, with $\Gamma_c = 4.0$ and $k_c = 6.98$.

For $0.92 \leq p \leq 0.95$, we find in our experiments a bicritical region where a complicated mixed mode surface pattern appears. These kind of patterns can arise from the nonlinear interactions of two or more linear instabilities [20, 21, 22, 23, 24]. They are often obtained by introducing frequency components in the forcing function with simple linear responses that interact in the horizontal plane to produce new structures. In contrast, in the current situation the changes in the tongue envelope selects linear instabilities that are not directly connected to the forcing components, and therefore the patterns generated through this mechanism could potentially be different. Unfortunately, in our current experiment the mixed surface patterns include complicated interactions with the side walls due to the small size of the container. Their proper analysis will therefore require a much larger aspect ratio and is left for future work.

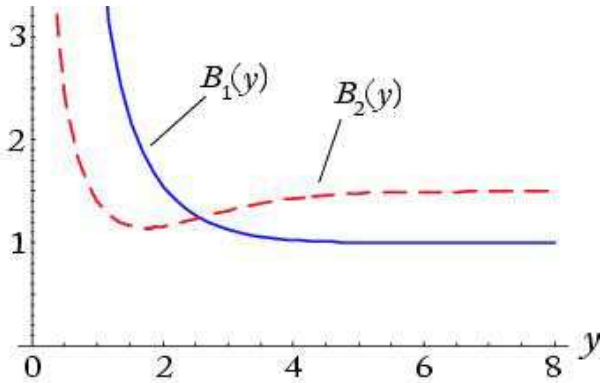


FIG. 4: (Color online) Plot of functions B_1 (solid line) and B_2 (dashed line), as defined by equations (16) and (17). Both functions diverge for $y \rightarrow 0$ with $B_1(y) \propto y^{-3}$ and $B_2(y) \propto y^{-1}$. For $y \rightarrow \infty$ they approach their corresponding asymptotic limits $B_1(y) \rightarrow 1$ and $B_2(y) \rightarrow 3/2$.

V. ANALYTICAL CALCULATIONS

A. The lubrication approximation

We are interested in exploring analytically the origin of the relation observed in Section III between $f(\omega t)$ and the envelope of $\Gamma_c(k)$. To proceed, we will focus on systems in the *lubrication regime*, where the ratio between the $\partial_t \vec{v}$ and the $\nabla^2 \vec{v}$ term of the Navier-Stokes equation is small. This ratio is of order $(l/\delta)^2$, where l is the distance that the fluid motion penetrates the surface and δ is the characteristic size of the boundary layer [28, 29, 35]. Since l can be estimated by either $1/k$ (if $kh \gg 1$) or h (if $kh \leq 1$), and δ is proportional to $\sqrt{\nu/\omega}$, it follows that a system is in the lubrication regime if it consists of a shallow enough fluid layer with high enough viscosity and a low enough oscillation frequency.

We use a simplified analytic description, introduced by Cerda and Tirapegui in [28, 29] for fluids under the lubrication approximation, in which a damped Mathieu equation involving only the motion of the free fluid surface is obtained. This equation is found by first deriving an exact non-local (in time) relation for the linear evolution of the surface, which is a formulation analogous to that developed in [36]. By imposing a short-memory to the system due to its fast dissipation rate, the non-local dependence is then neglected. The resulting Mathieu equation reads

$$\ddot{\xi}_k + 2\bar{\gamma}_k \dot{\xi}_k + \bar{\omega}_k^2 [1 + \Gamma_k f(\omega t)] \xi_k = 0, \quad (12)$$

where the dots represent derivatives with respect to time and

$$\bar{\gamma}_k = \nu k^2 B_1(kh) B_2(kh) \quad (13)$$

$$\bar{\omega}_k^2 = k [g + \sigma k^2 / \rho] B_2(kh) \quad (14)$$

$$\Gamma_k = \frac{\Gamma g}{g + \sigma k^2 / \rho}. \quad (15)$$

Here, $B_1(kh)$ and $B_2(kh)$ are explicit non-dimensional functions given by

$$B_1(y) = \frac{\cosh(2y) + 2y^2 + 1}{\sinh(2y) - 2y} \quad (16)$$

$$B_2(y) = \frac{3 \cosh^2(y) [\sinh(2y) - 2y - 4y^3/3] + y^2 [\sinh(2y) - 2y]}{[\sinh(2y) - 2y]^2} \quad (17)$$

Figure 4 shows that $B_1(y)$ and $B_2(y)$ have a simple structure despite their complicated algebraic expressions. As y approaches 0, both functions diverge with $B_1(y) \propto y^{-3}$ and $B_2(y) \propto y^{-1}$. For large values of y , $B_1(y)$ and $B_2(y)$ quickly converge to their asymptotic limits of 1 and $3/2$, respectively.

The critical forcing strength Γ_c can be found for every k by considering solutions of (12) that follow the Floquet form

$$\xi_k(t + 2\pi/\omega) = e^{\frac{2\pi}{\omega}(\mu + i\phi)} \xi_k(t), \quad (18)$$

and demanding that the growth rate after every period satisfies $\mu = 0$.

B. The WKB approximation

We will follow here the approach in [28, 29], which uses the well known (in the context of quantum mechanics) Wentzel-Kramer-Brillouin (WKB) approximation [30, 31] to solve the Mathieu equation. We first cast (12) into the form of a Schrödinger equation by defining

$$x = \omega t \quad (19)$$

$$\Psi(x) = \xi_k(x/\omega) e^{\bar{\gamma}_k x / \omega} \quad (20)$$

and

$$E = \bar{\omega}_k^2 - \bar{\gamma}_k^2 \quad (21)$$

$$V(x) = -\Gamma_k \bar{\omega}_k^2 f(x), \quad (22)$$

to obtain

$$\Psi''(x) + \frac{1}{\omega^2} [E - V(x)] \Psi(x) = 0, \quad (23)$$

where the double prime represents the second derivative with respect to x . The problem of finding the solutions of (12) that follow the Floquet form (18) then becomes equivalent to finding the eigenfunctions of (23) that satisfy

$$\Psi(x + 2\pi) = e^{\frac{2\pi}{\omega}(\mu + i\phi + \bar{\gamma}_k)} \Psi(x), \quad (24)$$

where the neutral stability curves are obtained for $\mu = 0$.

In regions where $\omega^2/|E - V(x)| \ll 1$, the WKB approximation provides explicit solutions for (23) which are divided into two different families. For $E < V(x)$ (as in the (a_j, b_j) -intervals of Fig. 5) they are given in their most general form by

$$\Psi(x) = \frac{1}{\sqrt{\omega P(x)}} \times \left\{ A \exp \left[\int_{x_0}^x P(\tilde{x}) d\tilde{x} \right] + B \exp \left[- \int_{x_0}^x P(\tilde{x}) d\tilde{x} \right] \right\} \quad (25)$$

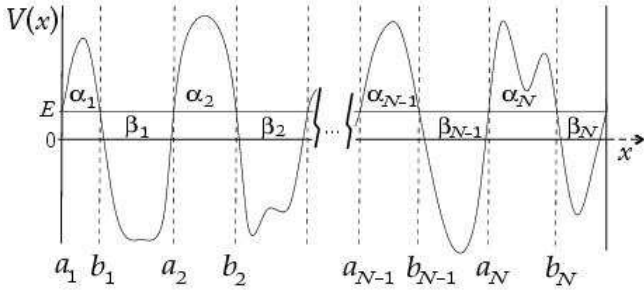


FIG. 5: Illustration of the intervals of $V(x)$ in which the integrals α_j and β_j are computed using expressions (31) and (32). In the WKB approach described (see text), a matrix M_j is defined through expression (30) for each (α_j, α_{j+1}) -interval.

and for $E > V(x)$ (intervals (b_j, a_{j+1}) in Fig. 5), by

$$\Psi(x) = \frac{1}{\sqrt{\omega P(x)}} \times \left\{ C \sin \left[\int_{x_0}^x P(\tilde{x}) d\tilde{x} \right] + D \cos \left[\int_{x_0}^x P(\tilde{x}) d\tilde{x} \right] \right\}. \quad (26)$$

Here, $P(x) = \sqrt{|E - V(x)|}/\omega$ and the complex constants A , B , C and D are obtained by imposing the boundary conditions in each segment. The solution for a given $V(x)$ over the full x domain is found by matching adjacent segments of $\Psi(x)$ at the points x_0 where $V(x_0) = E$. For $x \approx x_0$, however, expressions (25) and (26) are not valid and, following the WKB method, one must perform a matched asymptotic expansion around x_0 to find the correct matching formulas [31]. At the points $\{b_j\}_{j=1\dots N}$ shown on Fig. 5, these are given by

$$C = \frac{2A - B}{\sqrt{2}} \quad \text{and} \quad D = \frac{2A + B}{\sqrt{2}}, \quad (27)$$

and at the points $\{a_j\}_{j=1\dots N}$, by

$$A = \frac{C + D}{\sqrt{2}} \quad \text{and} \quad B = \frac{D - C}{2\sqrt{2}}. \quad (28)$$

We will now extend the neutral stability calculations carried out in [28, 29] for $V(x) \propto \cos(x)$ to arbitrary forcing functions. Imagine a periodic function $V(x)$ with $2N$ matching points per period as in Fig. 5. Using (27) and (28) we can relate the coefficients A_{j+1} and B_{j+1} of solution (25) in an interval (a_{j+1}, b_{j+1}) to the coefficients A_j and B_j in the previous interval (a_j, b_j) (see Fig. 5). We find

$$\begin{pmatrix} A_{j+1} \\ B_{j+1} \end{pmatrix} = M_j \begin{pmatrix} A_j \\ B_j \end{pmatrix}, \quad (29)$$

where the matrix M_j is defined by

$$M_j = \begin{bmatrix} 2e^{\alpha_j} \cos(\beta_j) & -e^{-\alpha_j} \sin(\beta_j) \\ e^{\alpha_j} \sin(\beta_j) & \frac{1}{2}e^{-\alpha_j} \cos(\beta_j) \end{bmatrix}, \quad (30)$$

with

$$\alpha_j = \int_{a_j}^{b_j} P(\tilde{x}) d\tilde{x} \quad (31)$$

$$\beta_j = \int_{b_j}^{a_{j+1}} P(\tilde{x}) d\tilde{x}. \quad (32)$$

The change in the amplitude of the wave function $\Psi(x)$ after a full period is therefore given by the product $M = M_N M_{N-1} \dots M_1$. Hence, for solutions with the Floquet form, equation (24) implies the neutral stability condition

$$\max(|\lambda_+|, |\lambda_-|) = e^{\frac{2\pi}{\omega} \bar{\gamma}_k}, \quad (33)$$

where λ_+ and λ_- are the two eigenvalues of M . An equivalent condition can be found by using the fact that the trace $\text{Tr}(M)$ is real and that the determinant $\text{Det}(M)$ is equal to 1, together with the standard relations $\text{Tr}(M) = \lambda_+ + \lambda_-$ and $\text{Det}(M) = \lambda_+ \lambda_-$. The resulting expression is

$$\text{Tr}(M) = \pm 2 \cosh \left(\frac{2\pi}{\omega} \bar{\gamma}_k \right), \quad (34)$$

where the plus or minus signs provide the neutral stability boundaries for harmonic or subharmonic resonances, respectively.

Note that for some values of k and Γ it is also possible to have $E > V(x)$ or $E < V(x)$ for all x , and therefore no intersections between $V(x)$ and E . In these situations the matrix M cannot be computed and our current implementation breaks down. However, the WKB method is still valid and it has been shown in [28, 29] that these cases never lead to instabilities. In our computation of the neutral stability curves we can therefore assume that there is at least one α and one β region per cycle.

C. Validity of the approximation.

We will investigate here the validity conditions for the approximation described above. The WKB method is based on an expansion in the small quantity $\omega^2/|E - V(x)|$ which can be estimated by [28, 29]

$$\frac{\omega^2}{|E - V(x)|} \sim \frac{\omega^2}{\bar{\gamma}_k^2} \sim \left(\frac{l}{\delta} \right)^4. \quad (35)$$

This criterion implies that the approximation should be valid for systems with $(l/\delta)^4 \ll 1$, which is a condition that must be satisfied in the lubrication regime in which we are focusing. Indeed, the lubrication regime requires $(l/\delta)^2 \ll 1$ and therefore, given that $(l/\delta)^4$ will be even smaller, the WKB approximation must also be valid in this regime. Let us estimate δ and l for the fluid parameters used in Sections III and IV. For surface waves oscillating at a frequency Ω_k , the characteristic size δ of the viscous boundary layer is of order $\sqrt{\nu/\Omega_k}$ [28, 29, 35].

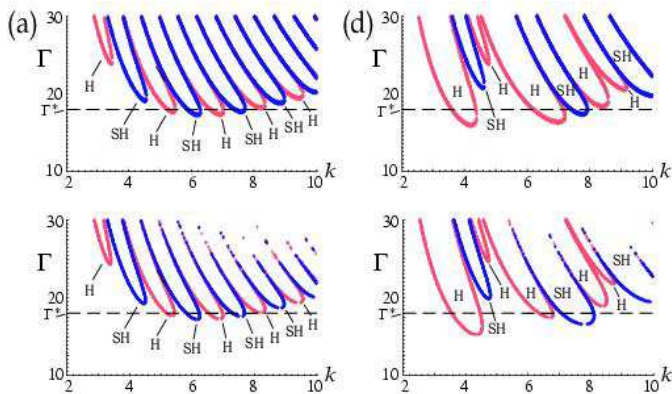


FIG. 6: (Color online) Neutral stability curves for a forcing function $f_p(\omega t)$ with (a) $p = -2$, (d) $p = 1$ (labeled as in Fig. 1) and parameters $\rho = 0.95 \text{ g/cm}^3$, $\sigma = 20 \text{ dyn/cm}$, $\nu = 46 \text{ cS}$, $\omega = 2\pi(3.5 \text{ Hz})$ and $h = 0.1 \text{ cm}$. Γ is in units of g and k in cm^{-1} . The exact numerical computations (top) are compared to the WKB approximation (bottom). The shape of the harmonic (H) and subharmonic (SH) resonance tongues is essentially identical for $p = -2$ and has similar characteristics for $p = 1$. In both cases, the tongues that would become unstable under a forcing of $\Gamma^* = 18$ (dashed line) coincide.

Since the response frequency of the dominant surface waves is typically of the same order as the forcing frequency, we have that $\delta \sim \sqrt{0.46/10} \approx 0.2 \text{ cm}$. On the other hand, the distance l that the motion of the surface penetrates the fluid can be estimated by the smallest value between $h = 0.3 \text{ cm}$ and $1/k$. In the region of k considered (see Fig. 6), l is therefore larger than $\sim 0.1 \text{ cm}$. Hence, for these parameters we have that l/δ is of order 1, which implies that the WKB method does not provide a good approximation.

In order to be able to use a WKB analysis in our study, we will consider in this section a shallower fluid layer with $h = 0.1 \text{ cm}$ and a lower oscillation frequency of 3.5 Hz , while keeping all other parameters unchanged. For this case, we have $\delta \sim \sqrt{0.46/3.5} \approx 0.4$, and $l \sim h = 0.1$. We thus obtain $(l/\delta)^4 < 10^{-2}$, which should imply a good WKB approximation. However, this criterion alone does not guarantee the accuracy of the resulting neutral stability curves. Indeed, for any forcing function there will be regions of x where $\omega^2/|E - V(x)| \gg 1$, in which (25) and (26) are not good approximations. Unfortunately, the effect of these regions over the full periodic $\Psi(x)$ solution cannot be easily estimated. This problem becomes even harder if $V(x)$ has a complicated shape because in such cases no simple approximation can even provide the number or size of these regions, which depend on k and Γ . We will therefore validate our analysis by directly comparing the WKB results to the numerical solutions of the full Navier-Stokes linear stability problem.

Figure 6 shows the neutral stability curves obtained using $\omega = 2\pi(3.5 \text{ Hz})$, $h = 0.1 \text{ cm}$ and the forcing function $f_p(\omega t)$ defined in expression (11) with $p = -2$ and $p = 1$ (labeled here ‘a’ and ‘d’, as in Fig. 1). The top

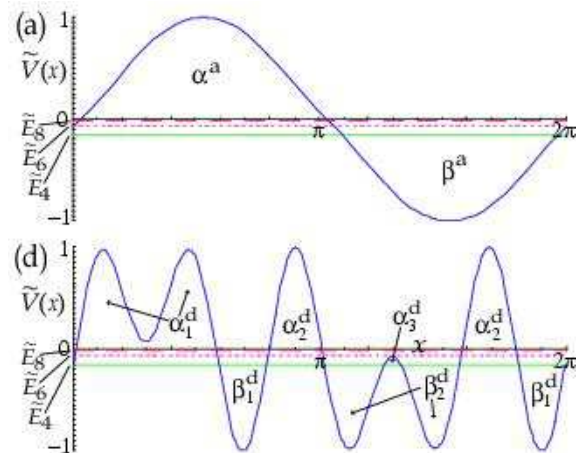


FIG. 7: (Color online) Integration regions for the WKB calculations pertinent to Figs. 8 and 9. The rescaled $\tilde{V}(x) = V(x)/(\Gamma_k \bar{\omega}_k^2)$ curves correspond to a forcing $f_p(x)$ with (a) $p = -2$ and (d) $p = 1$ (labeled as in Fig. 1). The values of $\tilde{E}_k = E/(\Gamma_k \bar{\omega}_k^2)$ are displayed for a forcing strength of $\Gamma^* = 18$ (see Fig. 6) at $k = 4$, $k = 6$ and $k = 8$. Note that the integration zone α_3^d is not present for \tilde{E}_6 and \tilde{E}_8 in (d).

panels show the exact numerical results computed using the method described in Section III, while the bottom ones present the approximate WKB solutions. The implementation of the WKB algorithm consists in finding the values $\Gamma_c(k)$ for which the trace of M satisfies (34), where M is obtained by multiplying the explicit expressions for M_j given in (30). By comparing the top and bottom panels, it is apparent that the WKB curves are almost indistinguishable from the exact results in the $p = -2$ case. For $p = 1$, the WKB approximation and the exact solution present a similar tongue structure but they do not coincide in the exact predicted values for the critical stability threshold of each tongue. However, the characteristics of their resonance tongue envelopes are the same. This is the relevant feature here since it is this envelope structure that we will study below using the WKB method.

D. Analysis of the envelopes

Using the WKB approximation, we are now in a position to relate the shape of the forcing function to the resonance tongue envelope. For any k and Γ , the stability criterion (34) can be computed in terms of

$$Q(k, \Gamma) \equiv \pm \frac{\text{Tr}(M)}{2 \cosh(2\pi\gamma_k/\omega)}, \quad (36)$$

where $Q(k, \Gamma) > 1$ indicates an instability. If the forcing function has only two extrema per cycle, there will always be at most one α and one β integration region, as illustrated on Fig. 7 (top) for $f_p(\omega t)$ with $p = -2$ (labeled by an ‘a’, as in Figs. 1 and 6). In these cases we

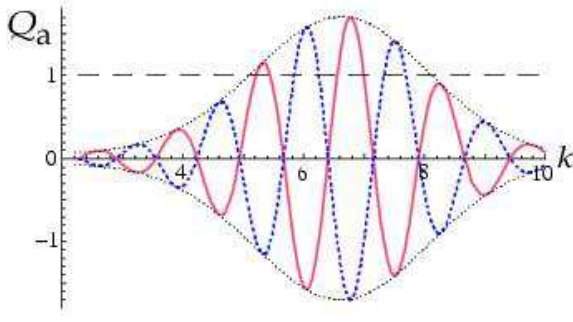


FIG. 8: (Color online) Plot of $Q_a(k, \Gamma^*)$ for a forcing function $f_p(\omega t)$ with $p = -2$ and a forcing strength Γ^* (see Fig. 6). The regions with $Q_a > 1$ are unstable with harmonic (solid curve) or subharmonic (dashed) responses. The dotted envelope is computed by discarding the $\cos(\beta^a)$ factor in equation (37).

have $M = M_1$, and (36) becomes

$$Q_a(k, \Gamma) = \pm \frac{\cosh(\alpha^a + \log 2) \cos(\beta^a)}{\cosh(2\pi\bar{\gamma}_k/\omega)}. \quad (37)$$

If we consider the function $Q_a(k)$ at constant Γ , the $\cos(\beta^a)$ factor will be responsible for oscillations that generate an unstable tongue at every excursion that reaches $Q_a > 1$. Figure 8 plots Q_a at a fixed forcing strength $\Gamma^* = 18g$, indicated by the dashed horizontal line on Fig. 6. The dotted lines trace the envelope of Q_a , which is readily obtained by discarding the $\cos(\beta^a)$ factor from (37). It exhibits a single maximum on the figure and for all other values of Γ tested, implying that the envelope of the resonance tongues must have a single minimum.

In contrast, forcing functions with multiple extrema produce more complicated envelope structures. Figure 9 shows a plot of $Q_d(k, \Gamma^*)$ for $f_p(\omega t)$ with $p = 1$ (labeled here Q_d since it corresponds to case ‘d’ in Figs. 1, 6 and 7). The oscillation amplitude presents two distinct zones of local maxima at $k \sim 4$ and $k \sim 7$, which are responsible for the two minima that the envelope of the resonance tongues displays in Fig. 6. In general, it is easy to see that any resonance tongue envelope with multiple minima must be associated with $Q(k)$ functions (at fixed Γ values) which have amplitude envelopes with multiple maxima. We will now study how these complicated amplitude envelopes arise by examining in detail the analytical form of Q_d .

The bottom panel of Fig. 7 shows the integration regions for the $p = 1$ case. Here, M is given by the product of either three or four matrices, depending on the k -interval considered, since the α_3 region is present for $k < \tilde{k} \approx 5.7$, but not for $k > \tilde{k}$. In the $k < \tilde{k}$ case it is straightforward to compute that

$$Q_d^<(k, \Gamma^*) \approx H_C^< C_1^< C_2^< + H_S^< S_1^< S_2^<, \quad (38)$$

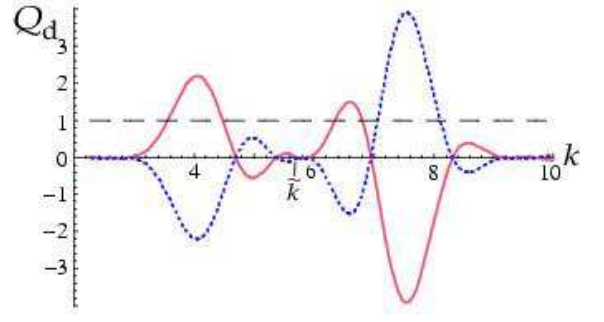


FIG. 9: (Color online) Plot of $Q_d(k, \Gamma^*)$ for a forcing function $f_p(\omega t)$ with $p = 1$ and a forcing strength Γ^* (see Fig. 6). The regions with $Q_d > 1$ are unstable with harmonic (solid curve) or subharmonic (dashed) responses. At \tilde{k} the definition of Q_d switches from $Q_d^<$ to $Q_d^>$, given by Eqs. (38) and (43), respectively, since the integration region α_3^d is not present for $k > \tilde{k}$ (see Fig. 7d).

with

$$H_C^<(k) = \frac{\cosh(\alpha_1^d + 2\alpha_2^d + \alpha_3^d + \log 16)}{\cosh(2\pi\bar{\gamma}_k/\omega)} \quad (39)$$

$$H_S^<(k) = \frac{\cosh(\alpha_1^d + 2\alpha_2^d - \alpha_3^d + \log 4)}{\cosh(2\pi\bar{\gamma}_k/\omega)}, \quad (40)$$

and

$$C_1^<(k) = \cos^2(\beta_1^d) \quad C_2^<(k) = \cos^2\left(\frac{\beta_2^d}{2}\right) \quad (41)$$

$$S_1^<(k) = -\sin^2(\beta_1^d) \quad S_2^<(k) = -\sin^2\left(\frac{\beta_2^d}{2}\right). \quad (42)$$

In (38), we have neglected several additional terms of a similar form, but where the argument of the hyperbolic cosine contained $-\alpha_1^d$ or $-\alpha_2^d$ contributions. These terms turn out to be negligible when compared to $H_C^<(k)$ and $H_S^<(k)$ since α_1 and α_2 are of the same order, and are much larger than α_3 (see Fig. 7d).

For $k > \tilde{k}$, M is composed of the product of only three matrices and the expressions become simpler. Using an equivalent approximation we obtain

$$Q_d^>(k, \Gamma^*) \approx H_C^> C_1^> C_2^>, \quad (43)$$

with

$$H_C^>(k) = \frac{\cosh(\alpha_1^d + 2\alpha_2^d + \log 8)}{\cosh(2\pi\bar{\gamma}_k/\omega)} \quad (44)$$

$$C_1^>(k) = \cos^2(\beta_1^d) \quad C_2^>(k) = \cos(\beta_2^d). \quad (45)$$

Figure 10 plots the H , C and S functions given above. After close examination, one finds that the structure of the envelope of $Q_d(k)$ is more complicated than that of $Q_a(k)$ mainly because of the interplay between the oscillating C and S terms. Indeed, the hyperbolic H terms behave similarly to the $Q_a(k)$ case, presenting only one local maximum, and are therefore not directly related to

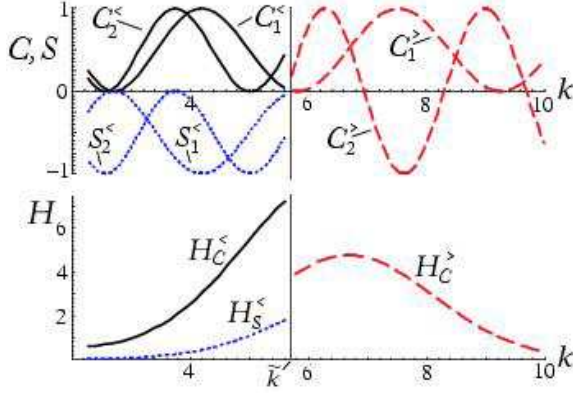


FIG. 10: (Color online) Main sinusoidal (top) and hyperbolic (bottom) components of the $Q_d(k, \Gamma^*)$ functions displayed in Fig. 9. Their combination through equations (38) and (43) (for $k < \tilde{k}$ and $k > \tilde{k}$, respectively) determines the amplitude envelope structure observed in Fig. 9.

the appearance of multiple extrema in the envelope. For example, at $k \approx 5$ both $H_C^<(k)$ and $H_S^<(k)$ grow with k but the envelope of $Q_d(k)$ decreases, mainly because of the oscillations of the $C_1^<C_2^<$ product. Note that the change in the number of integration regions at \tilde{k} is not essential either for obtaining multiple extrema: the combination of the oscillations of the C and S functions are able to produce additional extrema even beyond their corresponding domains. Furthermore, in various tested cases with different fluid parameters and forcing functions we have found no clear correlation between the changes in the number of integration regions and the shape of the neutral stability curves.

We now find analytic expressions that describe the envelope of the resonance tongues for any forcing function with only two extrema per cycle. The neutral stability criterion in these cases is equivalent to setting $Q_a(k, \Gamma) = 1$ in expression (37). By dropping the oscillatory factor $\cos(\beta^a)$ in (37) and using the high dissipation of the lubrication regime to neglect the $\log 2$ term (when compared to α^a which, for the parameters used in this section, is evaluated as $\alpha^a \approx 2\pi\bar{\gamma}_k/\omega \approx 300$), we find that

$$\alpha^a \approx \frac{2\pi\bar{\gamma}_k}{\omega} \quad (46)$$

at the envelope. Using the definitions of α^a and $\bar{\gamma}_k$, this condition can be rewritten as

$$\int_{V(x) > E} \sqrt{|1 - \chi + \Gamma_k(\chi) f(x)|} dx = 2\pi\sqrt{\chi}, \quad (47)$$

where the integration is carried out over the $V(x) > E$ region and the algebraic function $\chi(kh)$ is given by

$$\chi(y) = \frac{\kappa_1 y^3}{1 + \kappa_2 y^2} B_1^2(y) B_2(y), \quad (48)$$

with

$$\kappa_1 = \frac{\nu^2}{gh^3} \quad \text{and} \quad \kappa_2 = \frac{\sigma}{g\rho h^2}. \quad (49)$$

Equation (47) provides an implicit expression for $\Gamma_k(\chi)$ at the envelope. Using this result and the definition in (15), we find that the shape of the envelope of the resonance tongues under the current approximations is described by the function

$$\Gamma_e(kh) = [1 + \kappa_2 k^2 h^2] \Gamma_k(\chi(kh)). \quad (50)$$

Unfortunately, there appears to be no simple way to extract the properties of $\Gamma_e(kh)$ without further specifying κ_1 , κ_2 and $f(x)$. However, we have observed for all tested cases that if $f(x)$ has only two extrema per cycle, $\Gamma_e(kh)$ has only one minimum. While the validity of this statement for all cases is a conjecture that would require a proof which is beyond the scope of this paper, we consider below two simple examples where analytic progress can be made.

For square forcing (where $f(\omega t) = 1$ during half of the period and $f(\omega t) = -1$ during the other half), the conjecture can be proved as follows. First, we find the solution of (47)

$$\Gamma_k(\chi) = 3\chi + 1. \quad (51)$$

Then, we substitute this result into equation (50) to obtain an explicit expression for the envelope of the resonance tongues

$$\Gamma_e^{\text{sq}}(kh) = 3\kappa_1 k^3 h^3 B_1^2 B_2 + \kappa_2 k^2 h^2 + 1. \quad (52)$$

While the specific form of Γ_e^{sq} depends on the parameters κ_1 and κ_2 , its extrema can be readily computed by using $\partial_k \Gamma_e^{\text{sq}} = 0$. We find that they are located at the intersection of the functions $r(y) = -3 \partial_y [y^3 B_1^2(y) B_2(y)]$ and $s(y) = 2\kappa_2 y / \kappa_1$. Given that $r(y)$ does not depend on any parameters, it can be evaluated numerically without loss of generality. We find that it decreases monotonically, intersecting the $r = 0$ axis at $y^* \approx 1.479$. Using this result and the fact that $s(y)$ is a linearly increasing function, it is easy to see that $\Gamma_e^{\text{sq}}(kh)$ can have only one minimum (which must be located at $k \leq y^*/h$).

For triangular forcing, (where $f(\omega t)$ is a linear function that increases during half of the period and a decreases during the other half), the analytical calculation becomes much harder. The solution for Γ_k is given by the real root of the cubic equation

$$(\Gamma_k + \chi - 1)^3 = 9\Gamma_k^2 \chi. \quad (53)$$

It has a more complicated structure than (51), which renders the use of the techniques developed for the square forcing case impossible. In the current analysis we will therefore content ourselves with scanning the parameter space numerically to show that, for a wide range of systems with triangular forcing, the envelope of the resonance tongues has only one minimum. In order to do

this, we first note that the problem now depends on only two nondimensional parameters: κ_1 and κ_2 . We also note that we can write the analytic solution of (53) and use (48) and (50) to obtain a (very long) explicit algebraic expression for the envelope of the resonance tongues, which we label $\Gamma_e^{\text{tri}}(kh)$ but do not reproduce here because of its length. By evaluating $\partial_k^2 \Gamma_e^{\text{tri}}(kh)$ at 10^3 points between $k = 0$ and k -values that reach an asymptotic regime, using approximately 10^4 different (logarithmically spaced) combinations of the parameters $\kappa_1 \in [10^{-6}, 10^1]$ and $\kappa_2 \in [10^{-5}, 10^3]$, we find that $\Gamma_e^{\text{tri}}(kh)$ is always a smooth function with positive concavity. This strongly suggests that $\Gamma_e^{\text{tri}}(kh)$ has only one minimum and that the conjecture also holds for triangular forcings.

Finally, for a sinusoidal forcing $f(\omega t) \propto \cos(\omega t)$ one can only express $\Gamma_k(\chi)$ in terms of an integral equation which cannot be explicitly solved. The work in [28, 29], however, shows that $\Gamma_e^{\text{sin}}(kh)$ again appears to have only one minimum for any combination of parameters.

The results presented above relate the shape of the forcing function to that of the envelope of the resonance tongues. In particular, they support the conjecture that only a forcing with more than two extrema per cycle can generate a tongue envelope that has more than one minimum. A full proof of this conjecture would be of interest not only as a mathematical result, but also as a guide for engineering surface patterns. It would imply, for example, that only forcing functions that have this characteristic can display bicritical points involving non-contiguous resonance tongues.

VI. DISCUSSION AND CONCLUSIONS

We have presented a new approach for studying the effect of the shape of the forcing function on the Faraday linear surface wave instabilities. Through a numerical, experimental and analytic investigation, we have established a relation between the number of extrema in the forcing function and the number of minima that can appear in the envelope of the resonance tongues. This approach does not rely on a multi-frequency description of the forcing function. It therefore allows us to consider forcings that cannot be defined by the superposition of a few sinusoidal terms, but that can excite surface wave instabilities in new ways that could lead to a greater control of the surface patterns.

The analysis that we have carried out provides new insights for understanding the effects of the energy feeding mechanism in pattern forming systems. Indeed, we use the lubrication approximation to reduce the system to one degree of freedom and then apply the WKB method, which neglects the fast oscillations by integrating their net effect over the different forcing segments. By doing this, we achieve a description that is somehow similar to the simple mechanical analogies (with balls, springs and pendula) that are used in reduced dimensionality models of parametric resonance. In this context, it would be interesting to try to relate the simplified dynamics that the WKB calculations furnish for each wavenumber to the forcing strength required to reach its corresponding instability threshold. Furthermore, it may be possible to follow a similar approach to study the effects of the forcing mechanism in other fluid regimes or even in a different system, such as the granular Faraday experiments where strongly non-sinusoidal forcings is the norm [37].

From an analytical perspective, various additional connections between the forcing shape and the resonance tongues could be obtained by developing the implicit relations established here. We expect to be able to achieve this by adequately choosing a reduced set of forcing functions and using the right approximations. Obtaining these additional connections could lead to a better understanding of the inverse problem, in which the forcing function would be tailored to achieve a given instability.

From an experimental perspective, the lubrication regime in which our analytic results are obtained has not yet been widely explored. This is not due to any fundamental limitation but rather to technical difficulties, mainly in achieving high enough accelerations at low frequencies and having a large enough container for the surface patterns to develop. However, given that we obtain good analytical approximations in this regime, we hope that new experiments will explore this regime. This, together with an extension of our analysis to consider nonlinear effects, would allow an exploration of the patterns that can be formed by the linear instabilities achieved through the forcing function control.

VII. ACKNOWLEDGMENTS

MS acknowledges partial support from NASA Grant NAG3-2364 and NSF Grant DMS-0309667.

-
- [1] J. Miles and D. Henderson, *Annu. Rev. Fluid Mech.*, **22**, 143-165, (1990).
 - [2] M. C. Cross and P. C. Hohenberg, *Rev. Mod. Phys.*, **65**(3), 851-1112, (1993).
 - [3] A. Kudrolli and J. P. Gollub, *Physica D*, **97**, 133-154, (1996).
 - [4] B. Christiansen, P. Alstrom and M. T. Levinsen, *Phys. Rev. Lett.*, **68**(14), 2157-2160, (1992).
 - [5] B. Christiansen, P. Alstrom, M. T. Levinsen, *J. Fluid Mech.*, **291**, 323-341, (1995).
 - [6] C. Wagner, H. W. Müller and K. Knorr, *Phys. Rev. E*, **62**, R33-R36, (2000).
 - [7] D. Binks and W. van de Water, *Phys. Rev. Lett.*, **78**, 4043-4046, (1997).
 - [8] W. S. Edwards and S. Fauve, *Phys. Rev. E*, **47**, R788-R791, (1993).

- [9] W. S. Edwards and S. Fauve, *J. Fluid Mech.*, **278**, 123-148, (1994).
- [10] H. Arbell and J. Fineberg, *Phys. Rev. Lett.*, **84**, 654-657, (2000).
- [11] A. Kudrolli, B. Pier and J. P. Gollub, *Physica D*, **123**, 99-111, (1998).
- [12] H. Arbell and J. Fineberg, *Phys. Rev. Lett.*, **81**, 4384-4387, (1998).
- [13] H. W. Müller, *Phys. Rev. Lett.*, **71**, 3287-3290, (1993).
- [14] H. Arbell and J. Fineberg, *Phys. Rev. Lett.*, **85**, 756-759, (2000).
- [15] H. Arbell and J. Fineberg, *Phys. Rev. E*, **65**, 036224, (2002).
- [16] W. Zhang and J. Viñals, *J. Fluid Mech.*, **336**, 301-330, (1997).
- [17] P. Chen and J. Viñals, *Phys. Rev. Lett.*, **79**, 2670-2673, (1997).
- [18] M. Silber and A. C. Skeldon, *Phys. Rev. E*, **59**, 5446-5456, (1999).
- [19] P. Chen and J. Viñals, *Phys. Rev. E*, **60**, 559-570, (1999).
- [20] M. Silber, C. M. Topaz and A. C. Skeldon, *Physica D*, **143**, 205-225, (2000).
- [21] C. M. Topaz and M. Silber, *Physica D*, **172**, 1-29, (2002).
- [22] J. Porter, C. M. Topaz and M. Silber, *Phys. Rev. Lett.*, **93**, 034502, (2004).
- [23] J. Porter and M. Silber, *Physica D*, **190**, 93-114, (2004).
- [24] C. M. Topaz, J. Porter and M. Silber, *Phys. Rev. E*, **70**, 066206, (2004).
- [25] K. Kumar, *Proc. R. Soc. Lond. A*, **452**(1948), 1113-1126, (1996).
- [26] H. W. Müller, H. Wittmer, C. Wagner, J. Albers and K. Knorr, *Phys. Rev. Lett.*, **78**(12), 2357-2360, (1997).
- [27] T. Besson, W. S. Edwards and L. S. Tuckerman, *Phys. Rev. E*, **54**(1), 507-513, (1996).
- [28] E. Cerda and E. Tirapegui, *Phys. Rev. Lett.*, **78**(5), 859-862, (1997).
- [29] E. A. Cerda and E. L. Tirapegui, *J. Fluid Mech.*, **368**, 195-228, (1998).
- [30] A. Messiah, North Holland, (1961).
- [31] I. I. Goldman and V. D. Krivchenkov, Dover Publications Inc., New York, (1961).
- [32] K. Kumar, and L. S. Tuckerman, *J. Fluid Mech.*, **279**, 49-68, (1994).
- [33] Wolfram Research, Inc. Mathematica, Version 4.2. Champaign, Illinois, (2002).
- [34] W. Z. Chen and R. J. Wei, *Phys. Rev. E*, **57**(4), 4350-4353, (1998).
- [35] L. D. Landau and E. M. Lifshitz, Pergamon, (1987).
- [36] J. Beyer and R. Friedrich, *Phys. Rev. E*, **51**(2), 1162-1168, (1994).
- [37] F. Melo, P. B. Umbanhowar and H. L. Swinney, *Phys. Rev. Lett.*, **75**, 3838-3841, (1995).